Journal of Computer and Communications, 2024, 12, 318-331
https://www.scirp.org/journal/jcc
ISSN Online: 2327-5227
ISSN Print: 2327-5219

# A Low-Profile Aperture-Shared Dual-Band Circularly Polarized Antenna Based on Fabry-Pérot Cavity and Folded Reflect Array

**Jiafeng Hu**

School of Physics and Electronic Science, East China Normal University, Shanghai, China
Email: jia_feng_hu@163.com

**How to cite this paper:** Hu, J.F. (2024) A Low-Profile Aperture-Shared Dual-Band Circularly Polarized Antenna Based on Fabry-Pérot Cavity and Folded Reflect Array. *Journal of Computer and Communications*, **12**, 318-331.
https://doi.org/10.4236/jcc.2024.1212017

**Received:** December 10, 2024
**Accepted:** December 27, 2024
**Published:** December 31, 2024

## Abstract

This paper proposes a low-profile, aperture-shared dual-band bidirectional circularly polarized (CP) antenna. The design incorporates a partially reflective surface (PRS) and a multifunctional transmission-reflection integrated metasurface, enabling the integration of CP Fabry-Pérot cavity antenna (FPCA) and CP folded reflectarray (FRA), while preserving circular polarization purity and delivering high gain performance. In this design, the PRS acts as the reflector for the FRA at 8 GHz, while the multifunctional metasurface serves as the reflector for the FPCA at 8 GHz and provides phase compensation for the FRA at 13 GHz. Consequently, the FPCA and FRA can share the same aperture with high aperture reuse efficiency. The antenna achieves high gain across both frequency bands, with peak gains of 19.4 dBic and 22.8 dBic, respectively, without complex feeding networks. Leveraging the advantage of low focal-length-to-diameter ratio of the FRA, the array's profile is reduced, with a height-to-diameter ratio of only 0.46.

## Keywords

Aperture-Shared, Low-Profile, Circularly Polarized, Dual-Band, Fabry-Pérot Cavity Antenna, Folded Reflectarray

## 1. Dual-Band Structure-Shared Antenna

The rapid advancement of wireless communication technology and increasing demand for spectral efficiency have propelled multiband antennas to the forefront of future high-speed communications [1]. Aperture-shared antennas, designed to enable multiple antennas to operate simultaneously across different frequency bands within the same radiation aperture, have garnered significant attention from researchers [2]. These antennas offer the potential to substantially reduce the size of the antenna aperture and decrease manufacturing costs, thereby garnering widespread attention from researchers. Conventional aperture-sharing antennas achieve functionality by directly integrating the high-frequency radiation aperture into that of the low-frequency antenna [3] [4]. Given that high-frequency antennas are typically smaller than antennas working in lower band, this integration does not compromise the performance of low-frequency antennas. However, it is challenging to simultaneously achieve both low mutual coupling and a simple feeding structure. As a result, aperture-shared antennas designed using this approach often suffer from limited gain [5] [6].

In recent years, attributed to the characteristics of low-profile, simplified feeding network, and other advantages [7] [8], folded reflect array (FRA) and folded transmit array (FTA) have emerged as prominent candidates in applications requiring high gain and low-cost. By incorporating a polarization grid at the top and placing a sub-reflector with a feed antenna at the bottom, the electromagnetic waves propagating from the feed undergo two reflections between the polarization grid and the reflector, then are collimated by the reflector of FRA and the polarization grid of FTA, respectively. Based on ray-tracing principles, it is feasible to diminish the profile to 50% and 33.3% of the focal length for FRA and FTA [9] [10], respectively.

Fabry-Pérot cavity antenna (FPCA) has attracted increasing attention due to its simple structure, strong directionality, and high gain. FPCA typically comprises of a partially reflective surface (PRS) and a reflector with a feed interior to the cavity [11]-[13]. A small portion of the electromagnetic waves radiated from the feed source propagates through the PRS, while the majority is reflected. When the spatial separation between the PRS and the reflector satisfies specific conditions, the transmitted electromagnetic waves produce a constructive interference effect on the radiating aperture, significantly enhancing the antenna gain [14]. Therefore, FPCA holds promising applications in the field of aperture-shared antennas. In [15], a high-gain linearly polarized aperture-shared antenna structure combining FPCA and FRA is proposed, which comprises a transmit array (TA), a reflect array (RA), and a feed source integrated into the RA. The TA serves as the PRS of FPCA and the polarization grid of FRA in the low and higher band, respectively. To achieve circular polarized (CP) radiation, an aperture-shared antenna structure combining a CP RA and FPCA is proposed [16], based on a polarizer-integrated dual-function surface (PIDFS). However, because the RA employs a spatial feeding mechanism, the antenna has a relatively high overall profile. Additionally, the complex multi-layer polarization conversion structure introduces extra insertion loss to some extent [17].

For the purpose of reducing the profile of dual-band CP antenna, this work proposes a bidirectional aperture-shared dual-band CP antenna structure integrated with FPCA and FRA, which comprises a PRS, a multifunctional transmission-reflection integrated metasurface and a CP feed. The multifunctional metasurface acts as the reflector of the FPCA in the lower band and provides phase compensation for the FRA in the higher band. The FPCA and FRA share the same radiation aperture, achieving a high degree of integration, providing high gains of 19.4 dBic and 22.8 dBic at 8 GHz and 13 GHz, respectively and its height-to-diameter ratio is reduced to 0.46.

## 2. Basic Configuration and Principle of the Aperture-Shared Antenna Hybridizing FPCA and FRA

The fundamental arrangement and operating principle of the aperture-shared antenna structure is depicted in **Figure 1**. A partially reflective surface (PRS) is situated at the top, which comprises a metal layer, a metallic pattern and a dielectric substrate. A multifunctional transmission-reflection integrated metasurface located at bottom is designed to provide phase compensation for the FRA operating at a higher band (13 GHz), while maintaining the phase response of the lower band (8 GHz). It is constituted of two metallic patterns, two dielectric layers and a metal layer sandwiched between the dielectric layers. A dual-band right-hand circularly polarized (RHCP) planar feed is integrated at the center of the multifunctional metasurface.

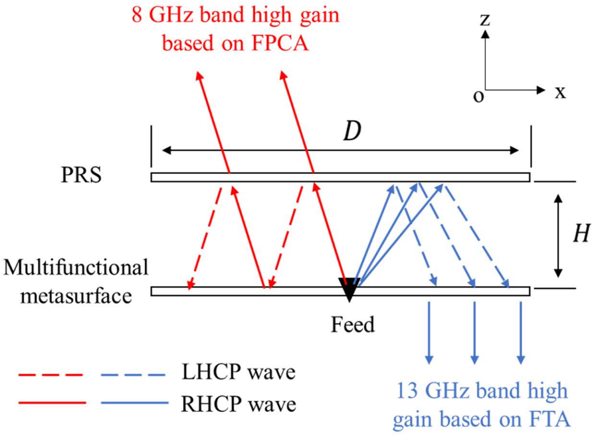

**Figure 1.** Configuration of the proposed aperture-shared antenna.

In the lower band (8 GHz), the multifunctional metasurface functions as the reflector which is essential to the FPCA configuration. The transmitted waves, upon interacting with the reflector and the PRS, undergo in-phase superposition, which effectively amplifies the radiation emitted from the aperture, thereby improving the directivity and gain of the antenna.

In the higher band (13 GHz), the multifunctional metasurface acts as a flat focusing lens. The operating principle is illustrated in **Figure 2**. RHCP spherical waves that radiated from the feed and propagating along the +*z*-direction, are reflected by the PRS, where their polarization is changed from RHCP to LHCP. These waves subsequently transmit through the bottom metasurface, with a reversal of polarization state (LHCP to RHCP), while being collimated into plane waves propagating along the -*z*-direction.

This approach achieves high-gain radiation at dual frequency bands. The distance ($H$) between the PRS and the multifunctional metasurface is half of the focal length.

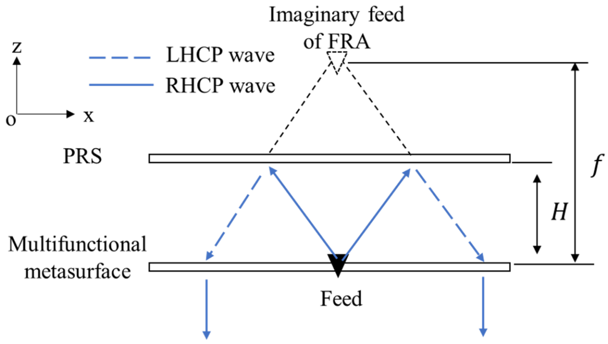

**Figure 2.** Operation principle of the proposed FRA at 13 GHz.

## 3. Dual-Band Aperture-Shared Antenna Design

This section introduces the structures of the unit cells of the PRS and multifunctional metasurfaces, with their operation performance validated through full-wave simulations. Additionally, the aperture and phase distribution of the proposed metasurface are presented.

### 3.1. Design of the Unit Cell of PRS

According to the theory proposed in [11], for the purpose of achieving constructive interference of electromagnetic waves emitted from the resonant cavity for high gain, the following equation should be satisfied:

$$\varphi_{PRS} + \varphi_{REF} = 4\pi h/\lambda - 2N\pi, N = 0, \pm 1, \pm 2\ldots \tag{1}$$

where $h$ is the height of the resonant cavity, $\varphi_{PRS}$ and $\varphi_{REF}$ denote the reflection phases of the PRS and the reflector, respectively. As a pivotal component of the FPCA, the PRS significantly influences its directivity. Given the assumption of an infinitely sized resonant cavity, the directivity $D$ of FPCA can be derived as follows [18]:

$$D = (1 + R)/(1 - R). \tag{2}$$

where $R$ represents the reflection magnitude of the PRS unit cell. **Figure 3** illustrates the structure of the proposed unit cell of the PRS. The unit cell has a size of 12 × 12 mm$^2$. Two metallic patterns are etched on the upper and lower layers of a F4B substrate ($\varepsilon_r = 3.5$, $\tan\delta = 0.001$, thickness $h_1 = 0.8$ mm). **Figure 3(b)** presents the simulation model of the unit cell in the CST Microwave Studio environment. The unit cell is subjected to unit cell boundary conditions in the *x*-and *y*-plane, while the Floquet ports are established along the *z*-axis. In the simulation, the incident plane wave propagates in the +*z*-direction, with the majority being reflected by the metallic pattern at the bottom of the unit cell, and a minor portion coupling through the dielectric substrate to the metallic structure at top, subsequently radiating into free space.

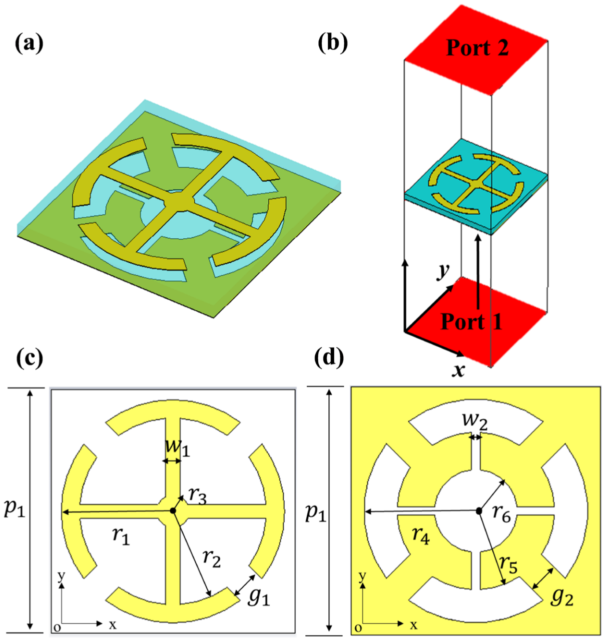

**Figure 3.** Geometries of the PRS unit cell (a) Perspective view (b) Simulation model of the unit cell in CST (c) Top view. (d) Back view.

According to Equation (2), increasing the reflection coefficient is conducive to enhancing the directivity of the FPCA. Therefore, it is necessary to adjust the parameters of the unit cell to achieve a high level of reflectivity. Initially, it is found that the reflectivity of the unit cell is significantly influenced by the parameter $r_1$. **Figure 4(a)** demonstrates the variation of the simulated reflection amplitude of the unit cell with respect to $r_1$. It is noticeable that when $r_1$ is set to 5 mm, a resonant peak is observed at 8.9 GHz, characterized by a sharp decrease in reflectivity. As $r_1$ increases from 5 mm to 5.5 mm, the resonance peak gradually shifts leftward, with the reflectivity at 8 GHz decreasing from 0.99 to 0.77. Upon further increment of $r_1$ to 6 mm, the resonance peak moves to the left of 8 GHz, resulting in an increase in the unit cell's reflectivity to 0.91.

The variation in $r_1$ also has an impact on the reflectivity of the unit cell within the 13 GHz band. As $r_1$ increases, the resonance peak in the higher band shifts progressively leftward, resulting in a decrease in reflectivity. When $r_1$ reaches 6 mm, the reflectivity at 13 GHz reduces to 0.22. Similarly, the influence of $r_4$ on the reflectivity of the unit cells is depicted in **Figure 4(b)**, which is analogous to that of r1. Consequently, the design must take into account the impacts of both $r_1$ and $r_4$ on both working frequency bands. Moreover, it is discovered that $g_1$ also significantly affects the reflectivity of the unit cell in the lower band. As depicted in **Figure 4(c)**, when $g_1$ increases from 0.5 to 2.5, the reflectivity around 8 GHz increases from 0.54 to 0.93, while having a negligible effect on the reflectivity near

13 GHz. In contrast to $g_1$, an increase in $g_2$ results in a noticeable improvement in reflectivity in the higher band, as demonstrated in **Figure 4(d)**.

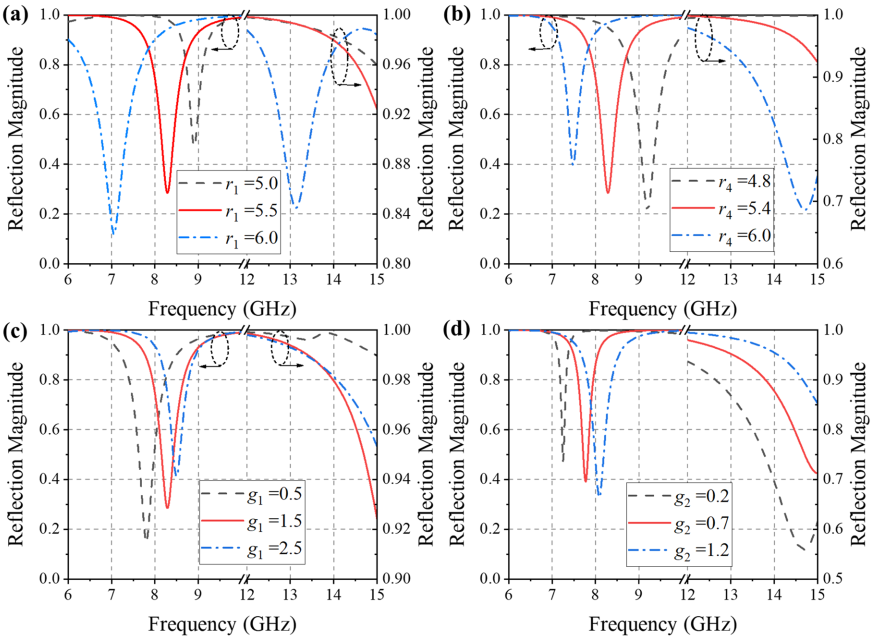

**Figure 4.** Effect of (a) $r_1$ (b) $r_4$ (c) $g_1$ (d) $g_2$ on the reflection magnitude $R_{LR}$ of the PRS unit cell.

Furthermore, as simulation results suggest that when the operating frequency bands are in the vicinity of the resonant peaks, variations in the angle of incidence can significantly affect the reflectivity and phase of the unit cell, it is necessary to adjust the parameters of the unit cell to achieve enhanced reflectivity, while ensuring the operation frequency bands remain at a considerable distance from the resonant peaks. Following optimization via full-wave electromagnetic simulations in CST Microwave Studio, the selected parameters are presented in **Table 1**.

**Table 1.** Parameters of the proposed PRS unit cell.

| Parameters | Value (mm) | Parameters | Value (mm) |
|---|---|---|---|
| $p_1$ | 12 | $r_4$ | 5.4 |
| $w_1$ | 0.7 | $r_5$ | 3.8 |
| $w_2$ | 0.4 | $r_6$ | 2 |
| $r_1$ | 5.5 | $g_1$ | 1.5 |
| $r_2$ | 4.6 | $g_2$ | 1.5 |
| $r_3$ | 0.8 | $h_1$ | 0.8 |

The frequency response of the PRS unit cell, as well as the variations in reflection coefficient under illumination from different incidence angles ($\theta$), are depicted in **Figure 5**. As demonstrated in **Figure 5**, the reflection amplitude of the unit cell varies between 0.9 and 0.8 around 8 GHz, ensuring the high gain of the Fabry-Pérot cavity structure. In the vicinity of 13 GHz, the magnitude of cross-polarized reflection of the unit cell approaches 1, meeting the reflective requirements for a reflector of the FRA structure.

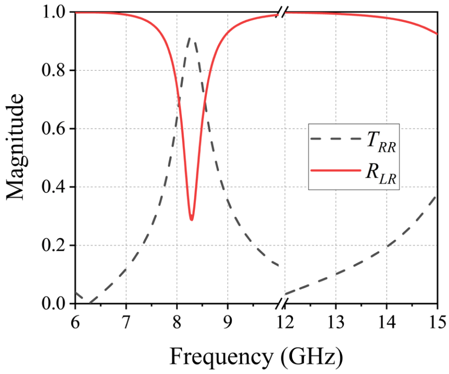

**Figure 5.** Frequency response of the PRS unit cell.

As indicated in **Figure 6(b)** and **Figure 6(c)**, within the 8 GHz frequency band, when $\theta$ increases from 0˚ to 50˚, the reflectivity of the unit cell decreases from 0.80 to 0.71, while the reflection phase exhibits a variation of 26˚. Within the 13 GHz frequency band, there is a decreasing trend in the reflectivity of the unit cells as the incidence angle increases, as illustrated in **Figure 7(a)**. Nonetheless, even when the incidence angle theta is raised to 50˚, the unit cell still maintains a reflectivity of approximately 0.82. Interferences during the phase compensation process are one of the crucial contributors to the reduction in gain and circular polarization purity of CP FRA. As evidenced in **Figure 7(b)**, in the higher band, when the incident angle $\theta$ increases from 0˚ to 50˚, the reflection phase of the unit cells increases from 171˚ to 184˚, with a phase difference of merely 13˚, indicating that the unit cell exhibits commendable phase stability, which is important in mitigating additional phase errors. In general, it can be observed that the unit cell maintains a comparatively stable reflective performance in both operation bands when $\theta$ is less than 40˚, thereby contributing to the enhancement of the gain of the FRA.

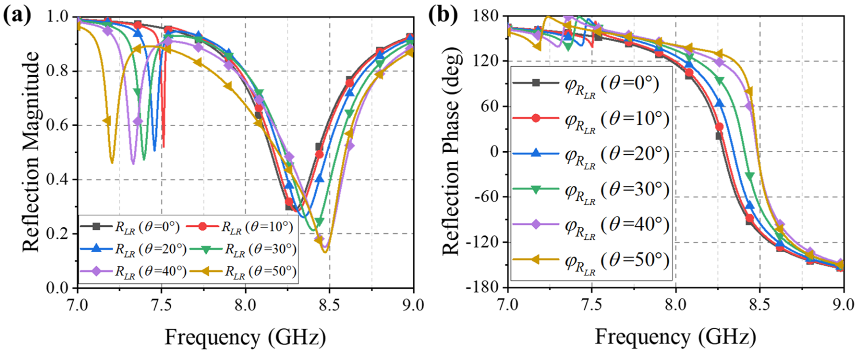

**Figure 6.** (a) Frequency response (b) Reflection phase versus different incidence angles of the PRS unit cell at 8 GHz.

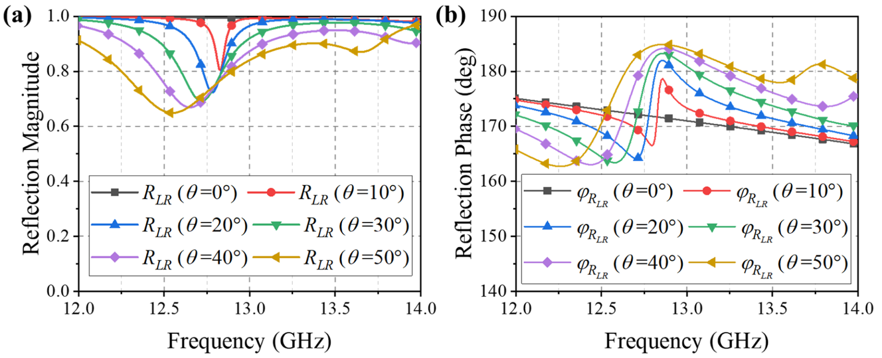

**Figure 7.** (a) Frequency response (b) Reflection phase versus different incidence angles of the PRS unit cell at 13 GHz.

### 3.2. Design of the Unit Cell of the Multifunctional Transmission-Reflection Integrated Metasurface

**Figure 8** illustrates the structure of the multifunctional transmission-reflection integrated metasurface element, which consists of two F4B substrates (thickness $h_2$ = 1 mm) separated by a 0.035 mm thick metallic surface. Two identical metallic patterns are printed on the top and bottom surfaces of the unit cell, respectively, as presented in **Figure 8(b)**. **Figure 8(c)** reveals that a slot with radius $r_c$ has been etched into the metallic ground plane to facilitate transmission function. The specific parameters of the element are detailed in **Table 2**. The frequency response of the element under RHCP wave incidence is depicted in **Figure 9(a)**. The unit cell achieves a reflectivity approaching 1 at 8 GHz and a transmissivity of 0.9 at 13 GHz. The variation of the transmission phase of the unit cell with respect to the rotation angle $a$ is shown in **Figure 9(b)**. With $a$ rotated from 0˚ to 180˚, a 360˚ phase shift is accomplished.

**Figure 10** illustrates the variation of phase with rotation angle of the unit at 13 GHz for different incidence angles ($\theta$). Within the range of $\theta$ = 0˚ - 40˚, the unit cell exhibits satisfactory amplitude and phase stability.

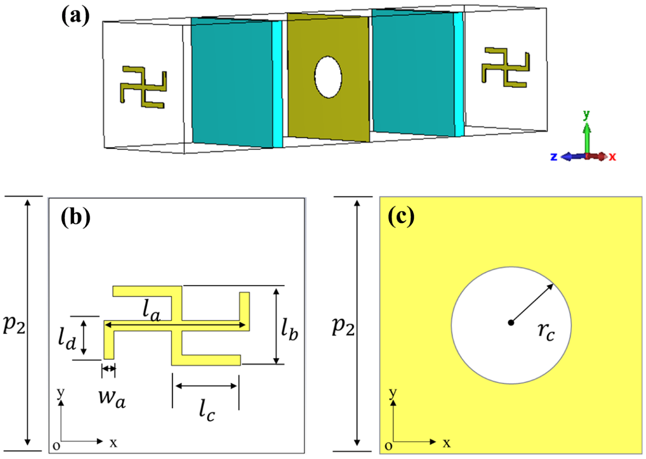

**Figure 8.** Geometries of the unit cell of the multifunctional metasurface (a) Perspective view in CST (b) Top view (c) Ground with a circular slot.

**Table 2.** Parameters of the proposed unit cell of the multifunction metasurface.

| Parameters | Value (mm) | Parameters | Value (mm) |
|---|---|---|---|
| $p_2$ | 10 | $l_b$ | 3.1 |
| $w_a$ | 1.4 | $l_c$ | 2.7 |
| $l_a$ | 5.7 | $l_d$ | 1.5 |
| $h_2$ | 1 | | |

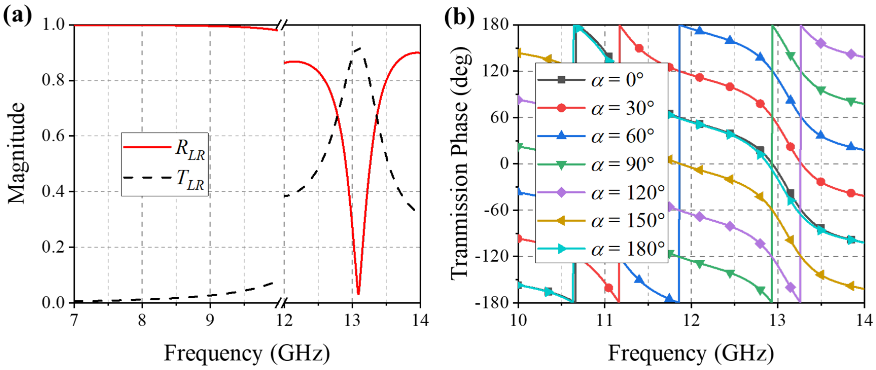

**Figure 9.** (a) Frequency response of the proposed unit cell; (b) Transmission phase of the proposed unit cell with different rotation angles *α*.

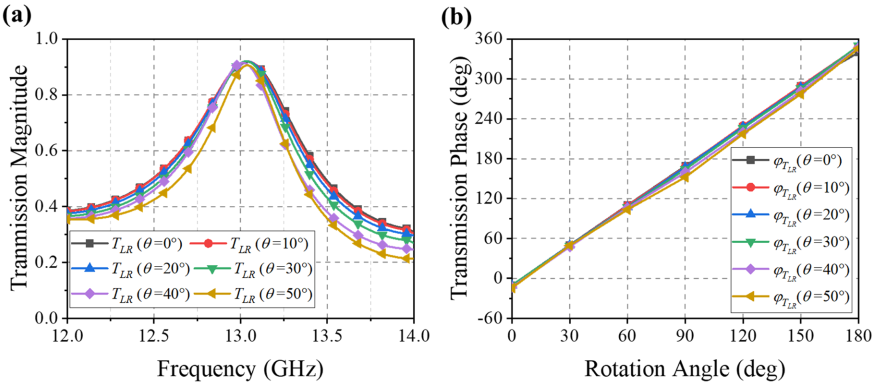

**Figure 10.** Transmission (a) Magnitude (b) Phase of the proposed unit cell under different incident angles *θ*.

### 3.3. Design of the PRS and Multifunctional Metasurface

In order to obtain a collimated beam, the refractive phase or reflection phase needs to follow a parabolic contour. The calculation of the required transmission phase distribution on the metasurface for focusing is as follows:

$$\varphi(x,y) = 2\pi\lambda^{-1}\left(\sqrt{x^2+y^2+f^2}-f\right)+\varphi_0. \tag{3}$$

By introducing the periodicity of the arrangement of units, Equation (3) can be transformed into a discretized form:

$$\varphi(m,n) = 2\pi p\lambda^{-1}\left(\sqrt{m^2+n^2+(f/p)^2}-f/p\right)+\varphi_0. \tag{4}$$

where $f$ is the focal length, $\varphi_0$ is the reference phase, and $\lambda$ signifies the operating wavelength in free space. Although increasing the aperture size of the high-gain antenna helps mitigate edge diffraction effects, it is essential to take the aperture efficiency of the antenna into account, which can be calculated as follows:

$$\eta = \left(G\lambda^2\right) / \left(4\pi A\right). \tag{5}$$

where $G$ represents the gain of the antenna, $\lambda$ denotes the operation wavelength in free space, and $A$ signifies the aperture area of the antenna. In this design, a low-profile bidirectional dual-band CP antenna is achieved by integrating a CP FPCA with a CP FRA within the same radiation aperture. According to Equation (1), the distance $H$ between the PRS and the multifunctional metasurface can be determined. Finally, after optimization employing CST Microwave Studio, $H$ is established as 95.1 mm. Then the focal length $f$ of the FRA is consequently determined, with the relationship $f = 2H$. Utilizing Equation (4), the aperture phase of the multifunctional metasurface at 13 GHz can be calculated. The phase distribution and arrangement of the multifunctional metasurface are illustrated in **Figure 11(a)** and **Figure 11(b)**, respectively.

In this design, the partial reflective surface and the multifunctional metasurface are constituted of 289 and 441 elements, respectively, with a total aperture size of 210 mm × 210 mm and height of 97.9 mm.

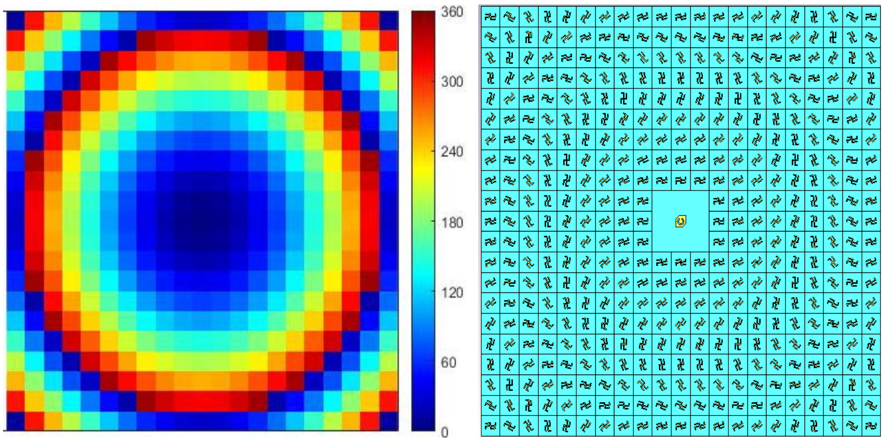

(a)

(b)

**Figure 11.** (a) Phase distribution; (b) Arrangement of the multifunctional metasurface.

## 4. Design and Simulation of the Aperture-Shared Antenna

To evaluate the performance of the antenna, a dual-band CP stacked patch antenna operating at 8 GHz and 13 GHz is designed, as shown in **Figure 12(a)**. The corresponding reflection coefficients and gains are illustrated in **Figure 12(b)**, with peak gains of 10 dBic and 9.6 dBic. By placing the stacked patch antenna at the center of the multifunctional metasurface as the feed source, the aperture-shared antenna is designed and simulated utilizing CST Microwave Studio.

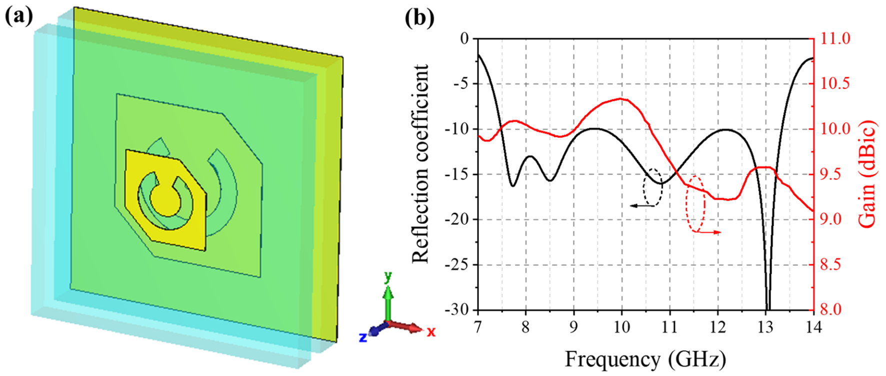

**Figure 12.** (a) 3-D sketch of the feed antenna in CST (b) Simulated reflection coefficient and gain of the feed antenna.

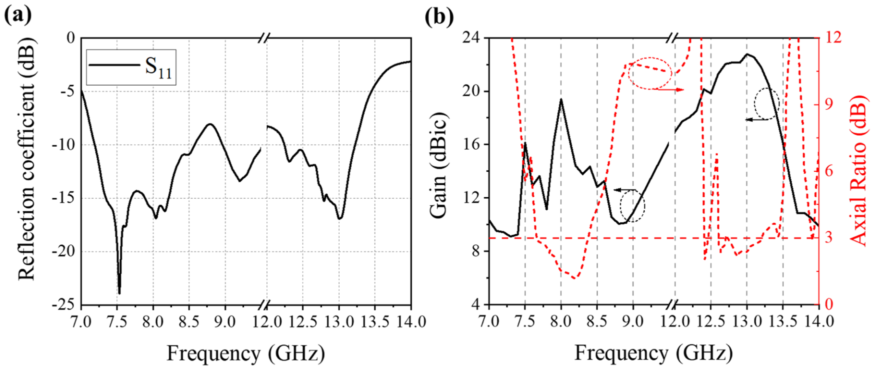

**Figure 13.** (a) Reflection coefficient (b) Gain and axial ratio of the proposed antenna.

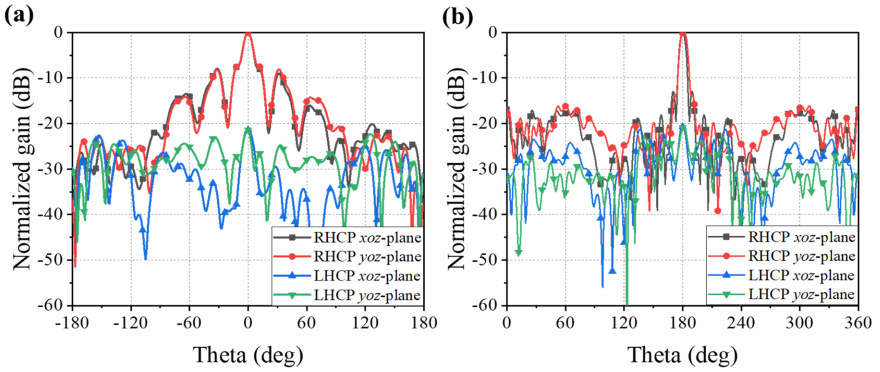

**Figure 14.** Simulated radiation patterns at (a) 8 GHz (b) 13 GHz.

The proposed antenna exhibits good impedance matching around 8 GHz and 13 GHz, with the -10 dB impedance bandwidths of 17.51% (7.19-8.57 GHz) and 7.94% (12.24-13.22 GHz), as shown in **Figure 13(a)**. The simulated gain and axial ratio (AR) of the aperture-shared antenna are displayed in **Figure 13(b)**. It can be observed that the simulated peak gains reach 19.4 dBic and 22.8 dBic at 8 and 13 GHz, with corresponding aperture efficiencies of 63.2% and 65.6%. Additionally, the 3 dB AR bandwidths of the antenna are 10.9% (7.58-8.45 GHz) and 8.4% (12.63 - 13.21 GHz) for the lower and higher bands, respectively. **Figure 14(a)** and

**Figure 14(b)** illustrates the simulated radiation patterns of the antenna in the *xoz*- and *yoz*-planes at 8 GHz and 13 GHz, respectively. The observation indicates that the antenna exhibits a cross-polarization level of approximately -20 dB.

**Table 3** provides a comparative analysis of the proposed antenna with other CP aperture-shared antenna designs. In contrast to recently proposed aperture-shared works, the proposed antenna exhibits a notable improvement in impedance matching bandwidth, particularly in the lower band, while maintaining competitive performance in terms of 3 dB AR bandwidth. Under similar frequency ratios and gain levels, the proposed antenna achieves nearly double the improvement in aperture efficiency compared to the design in [21] and offers up to 80% reduction in profile size compared to the antenna in [24].

**Table 3.** Comparison of different types of shared-aperture antennas.

| *Ref.* | Profile ($\lambda_{\text{low}}$) | Frequency Ratio | Peak Gain (dBic) | Impedance BW (%) | 3 dB AR BW (%) | Aperture Efficiency (%) |
|---|---|---|---|---|---|---|
| **[19]** | 0.05/0.08 | 1.5 | 5.1/5.4 | 4.5/10 | N.A. | N.A. |
| **[20]** | Single-layer Substrate | 1.4 | 17.5/18.3 | 8.3/18.9 | 14.2/14.9 | N.A. |
| **[21]** | 5.7/7 | 1.18 | 23.9/24.5 | 7.5/7 | 8.3/7.04 | 32.3/28.9 |
| **[22]** | 0.05/0.07 | 1.6 | 8.6/6.4 | 4.5/2.7 | 1.04/0.75 | 88.3/88.3 |
| **[23]** | 0.6/0.1 | 1.5 | 17.7/20.9 | 1.5/5.7 | 2.5/1.7 | 81.4/77 |
| **[24]** | 14.6/23 | 1.5 | 27.0/28.5 | 14.2/11.1 | 25/16.7 | 34.9/35.3 |
| **This work** | 2.6/4.2 | 1.625 | 19.4/22.8 | 17.51/7.94 | 10.9/8.4 | 63.2/65.6 |

## 5. Conclusion

In this work, through the integration of the FPCA with FRA, an aperture-shared bidirectional dual-band circularly polarized antenna characterized by low-profile and high gain, is designed and simulated utilizing CST Microwave Studio. Simulation results demonstrate that the antenna exhibits favorable reflection coefficients within the frequency bands of 7.19 - 8.57 GHz and 12.24 - 13.22 GHz, while maintaining good circular polarization purity across 7.58 - 8.45 GHz and 12.63-13.21 GHz. Moreover, the antenna exhibits dual-band high gain performance, its peak gains reaching up to 19.4 dBic at 8 GHz and 22.8 dBic at 13 GHz. The aperture efficiencies of the antenna are 63.2% and 65.6%, respectively. The antenna has an aperture size of $5.6\lambda_{\text{low}} \times 5.6\lambda_{\text{low}} \times 2.6\lambda_{\text{low}}$ with a height-to-diameter ratio of 0.46, making it highly promising for widespread application in wireless communication.

## Conflicts of Interest

The author declares no conflicts of interest regarding the publication of this paper.

## References

[1] Askarian, A. and Wu, K. (2023) Aperture-Shared Radiation Surface: A Promising Technique for Multifunctional Antenna Array Development. *Electromagnetic Science*, **1**, 1-20. https://doi.org/10.23919/emsci.2023.0008

[2] Pant, M. and Malviya, L. (2022) Design, Developments, and Applications of 5G Antennas: A Review. *International Journal of Microwave and Wireless Technologies*, **15**, 156-182. https://doi.org/10.1017/s1759078722000095

[3] Mao, C., Gao, S., Wang, Y., Chu, Q. and Yang, X. (2017) Dual-Band Circularly Polarized Shared-Aperture Array for C-/X-Band Satellite Communications. *IEEE Transactions on Antennas and Propagation*, **65**, 5171-5178. https://doi.org/10.1109/tap.2017.2740981

[4] Sun, Y., Leung, K.W. and Lu, K. (2021) Compact Dual Microwave/Millimeter-Wave Planar Shared-Aperture Antenna for Vehicle-to-Vehicle/5G Communications. *IEEE Transactions on Vehicular Technology*, **70**, 5071-5076. https://doi.org/10.1109/tvt.2021.3070353

[5] Xiang, B.J., Zheng, S.Y., Wong, H., Pan, Y.M., Wang, K.X. and Xia, M.H. (2018) A Flexible Dual-Band Antenna with Large Frequency Ratio and Different Radiation Properties over the Two Bands. *IEEE Transactions on Antennas and Propagation*, **66**, 657-667. https://doi.org/10.1109/tap.2017.2786321

[6] Xiao, F., Lin, X. and Su, Y. (2020) Dual-Band Structure-Shared Antenna with Large Frequency Ratio for 5G Communication Applications. *IEEE Antennas and Wireless Propagation Letters*, **19**, 2339-2343. https://doi.org/10.1109/lawp.2020.3032739

[7] Yang, P., Dang, R. and Li, L. (2022) Dual-Linear-to-Circular Polarization Converter Based Polarization-Twisting Metasurface Antenna for Generating Dual Band Dual Circularly Polarized Radiation in Ku-Band. *IEEE Transactions on Antennas and Propagation*, **70**, 9877-9881. https://doi.org/10.1109/tap.2022.3178803

[8] Lei, H., Liu, Y., Jia, Y., Yue, Z. and Wang, X. (2022) A Low-Profile Dual-Band Dual-Circularly Polarized Folded Transmitarray Antenna with Independent Beam Control. *IEEE Transactions on Antennas and Propagation*, **70**, 3852-3857. https://doi.org/10.1109/tap.2021.3125419

[9] Han, L., Zhu, Y., Xu, Y., Liu, Y., Xie, W. and Xiong, B. (2024) Novel Folded Reflectarray and Transmitarray Antenna Generating Long Nondiffractive Bessel Beams Carrying OAM with Integrated Feed. *IEEE Transactions on Antennas and Propagation*, **72**, 4719-4728. https://doi.org/10.1109/tap.2024.3383248

[10] Liu, W., Li, S., Chen, L., Zhang, C. and Deng, L. (2024) A Broadband High-Efficiency Spin-Decoupled Folded Transmitarray Antenna with Independent Beam Control. *IEEE Transactions on Antennas and Propagation*, **72**, 8058-8063. https://doi.org/10.1109/tap.2024.3445569

[11] Trentini, G.V. (1956) Partially Reflecting Sheet Arrays. *IRE Transactions on Antennas and Propagation*, **4**, 666-671. https://doi.org/10.1109/tap.1956.1144455

[12] Gardelli, R., Albani, M. and Capolino, F. (2006) Array Thinning by Using Antennas in a Fabry-Perot Cavity for Gain Enhancement. *IEEE Transactions on Antennas and Propagation*, **54**, 1979-1990. https://doi.org/10.1109/tap.2006.877172

[13] Liu, Z. (2009) Fabry-Perot Resonator Antenna. *Journal of Infrared, Millimeter, and Terahertz Waves*, **31**, 391-403. https://doi.org/10.1007/s10762-009-9605-4

[14] Xie, P., Wang, G., Li, H., Liang, J. and Gao, X. (2020) Circularly Polarized Fabry-Perot Antenna Employing a Receiver-Transmitter Polarization Conversion Metasurface. *IEEE Transactions on Antennas and Propagation*, **68**, 3213-3218.

https://doi.org/10.1109/tap.2019.2950811

[15] Liu, Z., Yin, R. and Lu, W. (2022) A Novel Dual-Band Shared-Aperture Antenna Based on Folded Reflectarray and Fabry-Perot Cavity. *IEEE Transactions on Antennas and Propagation*, **70**, 11177-11182. https://doi.org/10.1109/tap.2022.3195552

[16] Guo, Q., Chen, P., Liang, M., Sun, G. and Wu, G. (2024) A High-Gain Aperture-Shared Dual-Band Circularly Polarized Antenna Using Polarizer Integrated Dual-Functional Surface. *IEEE Transactions on Antennas and Propagation*, **72**, 6886-6896. https://doi.org/10.1109/tap.2024.3420123

[17] Dey, S. and Dey, S. (2024) Ultrathin Single Layer Transmissive Dual-Band Linear to Circular Converter for Non-Adjacent Dual Orthogonal Circularly Polarized Antenna. *IEEE Access*, **12**, 65981-65996. https://doi.org/10.1109/access.2024.3398144

[18] Liu, Z., Yin, R., Ying, Z., Lu, W. and Tseng, K. (2021) Dual-Band and Shared-Aperture Fabry-Perot Cavity Antenna. *IEEE Antennas and Wireless Propagation Letters*, **20**, 1686-1690. https://doi.org/10.1109/lawp.2021.3093575

[19] Smolders, A.B., Mestrom, R.M.C., Reniers, A.C.F. and Geurts, M. (2013) A Shared Aperture Dual-Frequency Circularly Polarized Microstrip Array Antenna. *IEEE Antennas and Wireless Propagation Letters*, **12**, 120-123. https://doi.org/10.1109/lawp.2013.2242427

[20] Zhang, J., Wu, W. and Fang, D. (2016) Dual-Band and Dual-Circularly Polarized Shared-Aperture Array Antennas with Single-Layer Substrate. *IEEE Transactions on Antennas and Propagation*, **64**, 109-116. https://doi.org/10.1109/tap.2015.2501847

[21] Cai, Y., Li, K., Li, W., Gao, S., Yin, Y., Zhao, L., *et al*. (2020) Dual-Band Circularly Polarized Transmitarray with Single Linearly Polarized Feed. *IEEE Transactions on Antennas and Propagation*, **68**, 5015-5020. https://doi.org/10.1109/tap.2019.2963594

[22] Ji, S., Dong, Y., Wen, S. and Fan, Y. (2021) C/X Dual-Band Circularly Polarized Shared-Aperture Antenna. *IEEE Antennas and Wireless Propagation Letters*, **20**, 2334-2338. https://doi.org/10.1109/lawp.2021.3110529

[23] Chang, X., Wang, H.B., Li, T.J., Jin, S.C., Liu, D.G. and Cheng, Y.J. (2022) Shared-aperture Phased Array Antenna with Codesigned Near-Field Coupled Circular Polarizer Loaded for K/Ka-Band Wide-Angle Satellite Communication. *IEEE Transactions on Antennas and Propagation*, **70**, 7478-7490. https://doi.org/10.1109/tap.2022.3196619

[24] Tong, X., Jiang, Z.H., Li, Y., Wu, F., Sauleau, R. and Hong, W. (2022) Dual-Wideband Dual-Circularly-Polarized Shared-Aperture Reflectarrays with a Single Functional Substrate for K-/Ka-Band Applications. *IEEE Transactions on Antennas and Propagation*, **70**, 5404-5417. https://doi.org/10.1109/tap.2022.3145484